Received: 28 July 2025 | Accepted: 23 October 2025

DOI: 10.1002/mgea.70038

RESEARCH ARTICLE

MGE ADVANCES
Materials Genome Engineering

Unveiling the influence of gravity on pitting corrosion through advanced high-throughput corrosion test method

Yiqi Zhou[1,2,3] | **Shuoyang Wang**[3] | **Shikang Feng**[4,5] | **Qingyang Liu**[6] | **Brahim Aissa**[6] | **Hussam Attar**[1,7] | **Sultan Mahmood**[8] | **Eguchi Kenichiro**[9]

[1]Metallurgy and Corrosion, Department of Materials, The University of Manchester, Manchester, UK

[2]Laboratory of Advanced Materials of Ministry of Education, School of Materials Science and Engineering, Tsinghua University, Beijing, China

[3]Beijing Advanced Innovation Center for Materials Genome Engineering, Institute for Advanced Materials and Technology, University of Science and Technology Beijing, Beijing, China

[4]Department of Materials, University of Oxford, Oxford, UK

[5]School of Engineering and Informatics, University of Sussex, Brighton, UK

[6]Materials Unit, Qatar Environment and Energy Research Institute, Hamad Bin Khalifa University, Doha, Qatar

[7]Research & Development Center, Saudi Aramco, Dhahran, Saudi Arabia

[8]Research & Innovation Centre, Capgemini Engineering, Toulouse, France

[9]Tubular Products & Casting Research Department, Steel Research Laboratory, JFE Steel Corporation, Tokyo, Japan

Correspondence
Yiqi Zhou.
Email: zhouyiqi@mail.tsinghua.edu.cn

Abstract

Bipolar electrochemistry is a high-throughput corrosion testing method capable of applying a quasi-linear potential gradient across test specimens. This study employs—bipolar electrochemistry corrosion testing to investigate the influence of gravity on pitting corrosion of type 304L and 420 stainless steel across a broad range of applied potentials. Gravity modifies the distribution of current density on the bipolar electrode without altering the potential distribution. The impact of gravity on pitting corrosion is achieved through its effects on the dilution of the electrolyte and the removal of the salt film within the pits. Pits oriented in a face up position demonstrate smoother morphologies, larger cross-sectional areas and pit volumes. In contrast, pits oriented in perpendicular and facedown positions exhibit pit shape. Under conditions governed by diffusion and activation control, pits can up to over 100 μm. Additionally, crystallographic pits are observed to form in areas subjected to high applied potentials.

1 | INTRODUCTION

In recent years, there has been a growing interest in high-throughput approaches for sample preparation, experimentation, and analytical methods, driven by their potential to save time and reduce material consumption.[1–7] However, conventional corrosion testing methods have limitations in simultaneously evaluating pitting corrosion nucleation and pit growth kinetics.[8–10] To address these challenges, bipolar electrochemistry has emerged as an innovative high-throughput corrosion testing technique. This method utilizes a bipolar electrode (BPE) to generate a quasi-linear potential gradient, allowing for simultaneous observation of various corrosion behaviors on the same sample in a single experiment.[11–14] Beyond facilitating varied corrosion responses, BPE provides a unique platform for investigating

critical pitting potential, pit growth kinetics, and the pit morphology over a wide range of potential.[14–20] Studies have revealed that pit depth remains independent of the applied potential, while larger and more open pits tend to form at higher applied potentials.[21,22] Furthermore, bipolar electrochemistry has been successfully applied to explore the evolution of de-alloying in brass and selective phase corrosion in hard-facing materials.[23,24]

Stainless steel is widely employed in various industrial applications owing to its exceptional mechanical properties and corrosion resistance.[25,26] However, stainless steel is susceptible to pitting corrosion, which is one of the most destructive and unpredictable forms of corrosion.[27] Pitting corrosion initiates with the localized breakdown of the passive film on the metal surface, leading to accelerated metal dissolution.[28] The pitting resistance is influenced by environmental factors such as temperature, electrolyte composition, and applied potential,[29] as well as by the chemical composition.[30,31] Pits typically nucleate at microstructural inhomogeneities, including inclusions,[32] carbides,[11] or phase boundaries.[33] The pitting process can be divided into nucleation, metastable propagation, and stable growth.[34] Metastable pit growth relies on the presence of a thin, porous cover over the pit, which acts as a diffusion barrier to maintain the local aggressive environment.[35] In contrast, stable pit growth is sustained by the pit volume (or pit depth), which serves as the diffusion barrier, enabling pit propagation without the porous cover.[36,37]

The concentration of metal cations is pivotal in the propagation of pits, with a critical threshold concentration (C_{surf}) being indispensable for the perpetuation of pit growth.[38] The pit electrolyte composition is contingent upon the dissolution of metal and the migration of metal cations from the pit's interior to the bulk solution. Should the concentration of metal cations at the pit's surface (C_{surf}) fall below the critical level (C_{crit}), re-passivation of the pit. Conversely, pit growth proceeds under activation control when C_{surf} reaches or exceeds C_{crit}. The peak dissolution current density of the metal at the pit surface ($i_{diss,max}$) must match the critical current density required for the outward diffusion of metal cations from the pit ($i_{diff,crit}$).[39,40] Nevertheless, the presence of a pit lacy cover can allow continued pit growth, with the dimensions of the cover's perforations influencing the expansion kinetics.[39] Upon the pit electrolyte attaining a critical concentration, a salt film is precipitated at the bottom of the pit,[41,42] which determines whether the pit continues to propagate or undergoes re-passivation.[43] The imperative of a salt film for consistent pit growth, however, remains controversial. Newman posited[36,44] that a salt film forms above the critical pitting temperature, facilitating stable pit growth. Contrarily, Li et al.[45] contended that salt film formation merely signifies pit growth under diffusion control and is not a prerequisite for stable pit growth. Galvele[46] emphasized the H^+ concentration as the critical factor for stabilizing pit growth, dismissing the necessity of a salt film. Additionally, Gaudet et al.[47] noted that pit growth is possible when the concentration of metal cations within the pit ranges from 60% to 80% of saturation.

The kinetics of pit growth are anticipated to vary with surface orientation due to the influence of gravity on pit electrolyte concentration and salt film stability. For face up (FU) orientated stainless steel, gravity facilitates the retention of aggressive pit electrolyte within the pit. In contrast, for perpendicular (PE) and face down (FD) orientated samples, gravity promotes the outward diffusion of the pit electrolyte, leading to the dilution of pit electrolyte.[48,49] Additionally, gravity plays a role in the salt film—stabilizing it in the FU orientation while removing it in the PE and FD orientations. Therefore, the morphology of pits is also significantly affected by gravitational forces. Sato et al.[50] demonstrated that under accelerated vertical gravity fields, the critical pitting potential decreased while the pit growth rate increased. Furthermore, open and elongated pits were observed to align with the direction of gravitational force in the samples.[48,49,51] Mankowski et al.[52] further investigated the evolution of pit morphology on samples with different surface orientations after being subjected to a constant potential of $+0.85\ V_{NHE}$ for up to 5 h. They reported that pits in the FU orientation were wider, whereas those in the FD orientation formed narrow ellipsoids, and the PE orientation exhibited pits with intermediate shapes. Notably, narrow pits were found to re-passivate more readily, as the challenge of ion diffusion was outweighed by the easier accumulation of aggressive pit electrolyte.[53]

In real-world components, pit nucleation is not restricted to FU orientations. Therefore, a practical goal of studying pit kinetics under varied conditions is to enable reliable prediction of a component's remaining useful life under specific operating conditions. Conventional electrochemical methods for studying the effect of gravity on pitting corrosion are typically constrained by the limited number of pits that can be statistically analyzed. The objective of this study is to use bipolar electrochemistry to investigate the development of pitting nucleation, propagation, and morphology of stainless steels (both with and without lacy pit covers) under different applied potentials during the growth phase under the influence of gravity based on few hundreds of pits, which overcome the traditional corrosion test methods, which the pit morphologies is obtained under one constant potential based on few numbers of pits. The stainless steel is positioned in three distinct orientations FU, PE, and FD—to simulate the effects of gravity on pitting corrosion. Two types of stainless steel, type 420 and type 304L, are selected for this investigation. Type 420 stainless steels do not form lacy pit covers during pit expansion, whereas type 304L stainless steel exhibits pits with lacy covers during the metastable growth.[21,54] In addition to the bipolar electrochemistry approach, 3-electrode potentio-dynamic and potentio-static polarization tests are conducted to compare the changes in pit nucleation and propagation under the influence of gravity. This comprehensive methodology provides deeper insights into the contribution of gravity to pitting corrosion behavior of stainless steels under a wide range of potentials.

2 | MATERIALS AND METHODS

The composition of Type 304L stainless steel (in wt%) was 18.4% Cr, 8.7% Ni, 0.02% C, 0.04% N, with the balance being Fe. Type 420 stainless steel comprised 13.7% Cr, 0.46% C, 0.47% Si, 0.39% Mn, and the remainder as Fe. Both Type 304L and 420 samples, with dimensions of 30 × 10 mm^2 (length × width), were prepared for 3-electrode potentio-dynamic and potentio-static polarization tests. The samples were electrically connected to the back-side of the exposed surface using copper wire, embedded in Araldite resin, and ground to a 1200-grit finish. The potentio-dynamic and potentio-static polarization curves were measured using a platinum electrode, a saturated calomel reference electrode (SCE), an IVIUM-Compactstat potentiostat, and IVIUMsoft software. After stabilizing the open circuit potential (OCP) for 30 min, the potentio-dynamic polarization test was conducted from −200 to +1000 mV versus OCP at a scan rate of 1 mV/s. To avoid crevice corrosion nucleation during the test, all four sides of the sample were ground to a 1200-grit finish before mounting in the resin. For the potentio-static polarization test, a constant potential of +300 and +500 mV_{SCE} was applied to the Type 420 and 304L stainless steel samples, respectively. For bipolar electrochemistry experiments, samples of the same dimensions 30 × 10 mm^2 and a thickness of 1–2 mm were mounted in Araldite resin. A plastic tube was attached to the backside of the exposed surface, and the samples were ground to a 1200-grit finish. Additionally, for microstructure analysis, the Type 420 BPE was polished to a 1 μm finish prior to bipolar exposure.

Figure 1a illustrates the experimental setup for bipolar electrochemistry, which employed a Keysight E36015A DC as the power supply. The surface area of platinum feeder electrodes is 4 cm^2. Oxidation reactions occurred on the BPE near the negative feeder electrode, while reduction reactions took place near the positive feeder electrode. The experiments were conducted using 0.1 and 0.05 M HCl as the electrolytes, and the distance between the two feeder electrodes was fixed at 70 mm. The BPE was positioned centrally between the feeder electrodes, and a voltage of 10 V was applied to the feeder electrodes. The bipolar electrochemistry experiments were performed in 5-min intervals, with individual samples removed after 5, 10, and 15 min of exposure to a 0.1 M HCl solution. To investigate the influence of gravity on pitting corrosion over extended periods, type 420 BPEs with different surface orientations were exposed to 0.05 M HCl for 120 min. Figure 1b shows the BPE configurations with FU, PE, and FD orientations, where the green-colored surfaces indicate the exposed areas. The FU stainless steel refers to the material with its exposed surface facing upward (toward the sky), while the FD material denotes the exposed surface facing downward (toward the earth). The PE specimen is positioned PE to the ground. Different surface orientation was achieved by bending the plastic tube.

The potential and current distribution across the BPE cannot be measured as there is no external electrical connection. A split BPE configuration was employed to determine the potential and current density distribution along the BPE.[8] The split array BPE electrode comprised 13 rectangular coupons, each measuring 1.9 × 10 mm^2 (length × width). Each segment was individually connected to a copper wire on the backside of the exposed surface, with insulation tape ensuring electrical isolation between adjacent segments. When assembled in sequence using the copper wire, these split BPEs collectively formed the dimensions of a single BPE electrode. To measure the local current at each segment, the coupons were connected to zero-resistance ammeters (ZRAs) via the copper wires. The ZRAs were used to record the current flowing from each segment BPE to the integrated BPE. For potential measurements, a Luggin probe was positioned approximately 1 mm above the BPE surface and connected to a SCE.

After stabilizing the OCP, the bipolar electrochemistry experiment was initiated. The local potential above the BPE was determined by calculating the difference between the recorded potential from Ivium potentiostat and the OCP value. The current values measured by the ZRAs represent

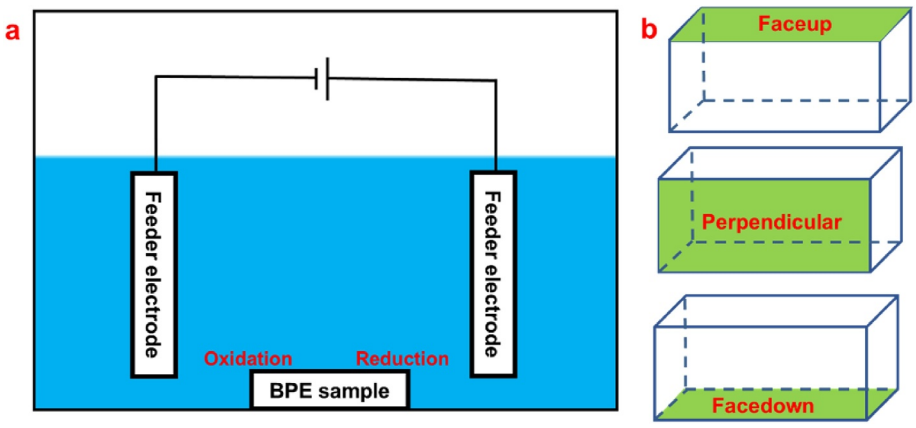

FIGURE 1 (a) Experimental setup for bipolar electrochemistry, with (b) the colored face of the BPE indicating the orientation of the exposed sample surface. BPE, bipolar electrode.

the current flow from each segment specimen to the entire BPE. Following the experiments, the BPEs were removed from the electrolyte, cleaned with soap, and subjected to an ultrasonic bath to collapse and remove the lacy pit covers for subsequent analysis of pit dimensions. The Keyence VK-200K microscopy system was used to determine the pit morphology. Additionally, the Zeiss Sigma VP FEG-SEM was employed for high-resolution SEM imaging of the pit morphology.

3 | RESULTS AND DISCUSSION

3.1 | Polarization test

The potentio-dynamic polarization test was employed to examine the change of E_{pit} across different surface orientations, while the propagation of stable pits was analyzed using a potentio-static polarization test. These potentials were approximately 0.2 V_{SCE} higher than the E_{pit}. As illustrated in Figure 2a, the potentio-dynamic polarization curves for type 420 stainless steel demonstrated consistent results across FU, PE, and FD orientations. The corrosion potential (E_{corr}) was approximately -0.5 V_{SCE}, and the current density was relatively high (exceeding 1 mA/cm^2), indicating the absence of a passive region. Due to the low chromium content (13 wt%) and a significant volume fraction of chromium carbides, the chromium concentration in the Type 420 stainless steel matrix is only slightly higher than the critical threshold (12.5 wt%), making it challenging to form a stable passive film in the HCl environment.[11] Figure 2b presents the potentio-dynamic polarization curves for type 304L stainless steel, revealing similar potentio-dynamic polarization behaviors across all samples. The corrosion performance of type 304L stainless steel was found to be superior to that of type 420 stainless steel, exhibiting higher E_{corr} (≈ -0.11 V_{SCE}) and E_{pit} ($\approx +0.33$ V_{SCE}). A distinct passive region was observed for Type 304L stainless steel, spanning from -0.2 to $+0.2$ V_{SCE}, with a passive current density of approximately 10^{-5} A/cm^2.

Figure 2c illustrates the current density response of type 420 stainless steel under different surface orientations at a constant potential of $+0.3$ V_{SCE}. For the FU orientation, the current density rapidly increased to 17 mA/cm^2 and then gradually rose to 20 mA/cm^2. For the PE and FD orientations, the current density quickly reached approximately 14 and 9 mA/cm^2, respectively. In Figure 2d, the current density for type 304L stainless steel at a constant potential of $+0.5$ V_{SCE} is compared across different surface orientations. Initially, the current density for all orientations was similar,

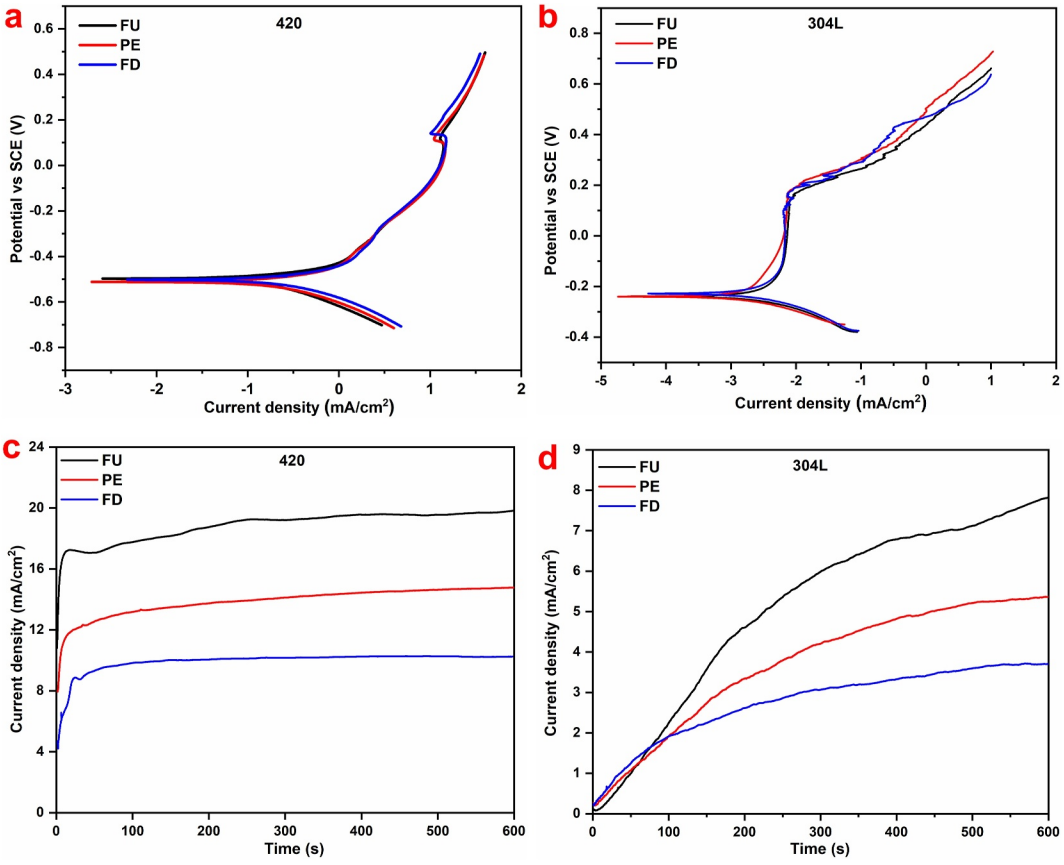

FIGURE 2 Potentio-dynamic polarization of type (a) 420 and (b) 304L stainless steel, with potentio-static polarization curves of type (c) 420 stainless steel at $+0.3$ V_{SCE} and (d) 340L stainless steel at $+0.5$ V_{SCE} in 0.1 M HCl.

around 2 mA/cm^2, within the first 100 s. However, from 100 to 600 s, the highest current density was observed in the FU orientation, while the lowest current density was recorded in the FD orientation. Significant crevice corrosion was observed at the interface between the stainless steel and the resin, indicating that the measured elevated current density is caused by a combination of localized corrosion (pitting and crevice corrosion) rather than pitting corrosion alone, however, the current density shows the contribution of gravity to localized corrosion kinetics.

3.2 | Potential and current distribution on the BPE

The potential and current density distributions on the type 304L BPE with FU, PE, and FD orientations are illustrated in Figure 3. The potential and current density at each point on the BPE were calculated as the average value over 10 min of bipolar exposure, and it was observed that the measured potential and current remained relatively stable over time. In Figure 3a, the potential distribution on the type 304L BPE with different surface orientations is presented. The maximum potential was approximately +0.8 V_{OCP} at the BPE oxidation edge, and the minimum potential was around −0.8 V_{OCP} at the BPE reduction edge. The potential exhibited a nearly linear distribution along the length of the BPE, with similar potential distributions observed for FU, PE, and FD orientations. Figure 3b illustrates the current density distribution on the type 304L BPE. For the BPE with PE and FD orientations, the current density distribution was similar, ranging from +5 mA/cm^2 at the BPE oxidation edge to −4 mA/cm^2 at the BPE reduction edge. However, a steeper current density distribution was observed for the BPE with the FU orientation, ranging from +10 to −10 mA/cm^2. The higher anodic current density observed in the FU orientation is attributed to more severe localized corrosion (involving both pitting and crevice corrosion). Consequently, to maintain charge neutrality, the boundary between the anodic and cathodic regions shifts, accompanied by an increase in the cathodic current density on the BPE's reduction side. The segmented bipolar electrochemical experiments reveal that the potential distribution on the BPE is independent of surface orientation, whereas gravity significantly influences the current distribution. The potential distribution on the type 304L BPE was found to be similar in FU, PE, and FD orientations. This consistency allows for the direct comparison of the critical pitting potential on the BPE at different surface orientations. Furthermore, the influence of gravity on pit growth kinetics and pit morphology can be directly assessed by comparing results at the same location on the BPE under different surface orientations. This approach provides a robust framework for evaluating the role of gravity in localized corrosion behavior, enabling a deeper understanding of how surface orientation affects the development and propagation of pits.

3.3 | Optical images of pitting region on the BPE

After bipolar electrochemistry testing on type 420 stainless steel, crevice corrosion, pitting corrosion, and general corrosion, were observed on the BPE. Figure 4 illustrates the regions covered by pits on the type 420 stainless steel BPE at different orientations over exposure times ranging from 5 to 15 min. While crevice corrosion was observed, it falls outside the scope of this study and will not be discussed further. All pits in type 420 stainless steel were open, with no evidence of lacy pit coverage. The pit covered length on the BPE means the distance between BPE oxidation edge and pit closest to BPE center. Longer pit coverage lengths corresponded to a lower critical pitting potential. Notably, scratches from grinding were observed on the BPE with PE and FD orientations but were absent in the FU orientation, as the aggressive pit electrolyte diffused out of the pit mouth and corroded the surrounding surface. For the FU orientation, gravity kept the pit electrolyte on the surface after diffusion out, leading to severe general corrosion.[22] In contrast, for the PE and FD orientations, gravity facilitated the departure of the pit electrolyte from the pit mouth after diffusion, resulting in less severe general corrosion. Additionally, in the PE orientation, black lines composed of pits were observed, representing the flow pathways of the pit electrolyte.

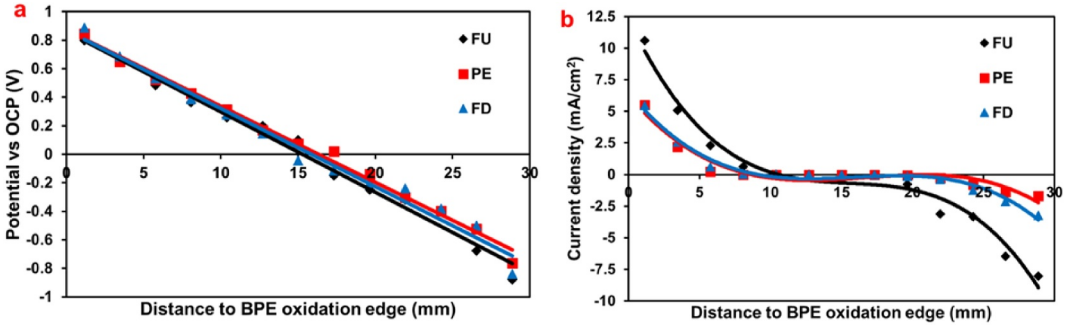

FIGURE 3 (a) Potential distribution and (b) current density distribution along the type 304L BPE with different surface orientations. BPE, bipolar electrode.

Crevice corrosion, pitting corrosion, and passivation + cathodic responses were observed on the type 304L BPE, as shown in Figure 5. The largest pits were located near the BPE oxidation edge, and the cross-sectional area of the pits increased with exposure times, indicating that higher applied potentials and extended exposure durations result in larger pit sizes. The pit covered length was longest in the BPE with the FU orientation, followed by the FD and PE orientations. Additionally, the pit size in the FU oriented BPEs was consistently larger than in the PE and FD oriented BPEs across all exposure times, indicating a faster pit growth kinetics in the FU orientation. According to the potentio-dynamic polarization curves (Figure 2), the E_{pit} is independent of surface orientation. However, pit covered length on BPE varies with surface orientation. For type 304L stainless steel, the covered length of pit follows the order FU > FD > PE. This discrepancy arises from the different electrochemical test conditions between the two methods. In bipolar electrochemistry, the

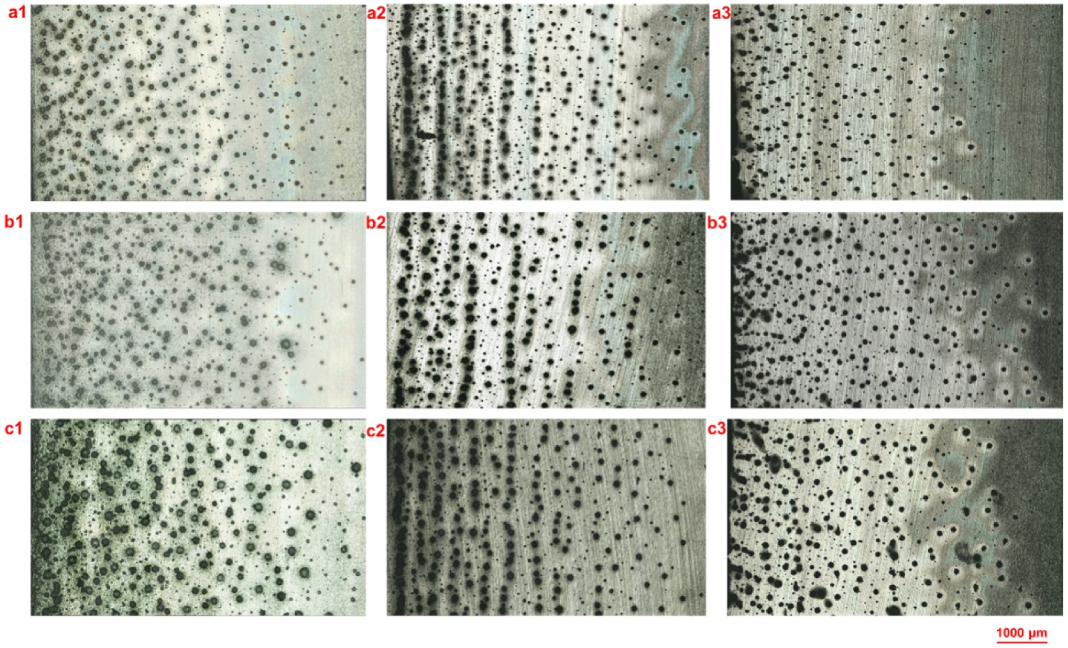

FIGURE 4 Pitting covered length on the type 420 BPE with different surface orientation (1. FU, 2. PE, and 3. FD) for varies exposure time (a) 5 min, (b) 10 min, and (c) 15 min. BPE, bipolar electrode; FD, face down; FU, face up; PE, perpendicular.

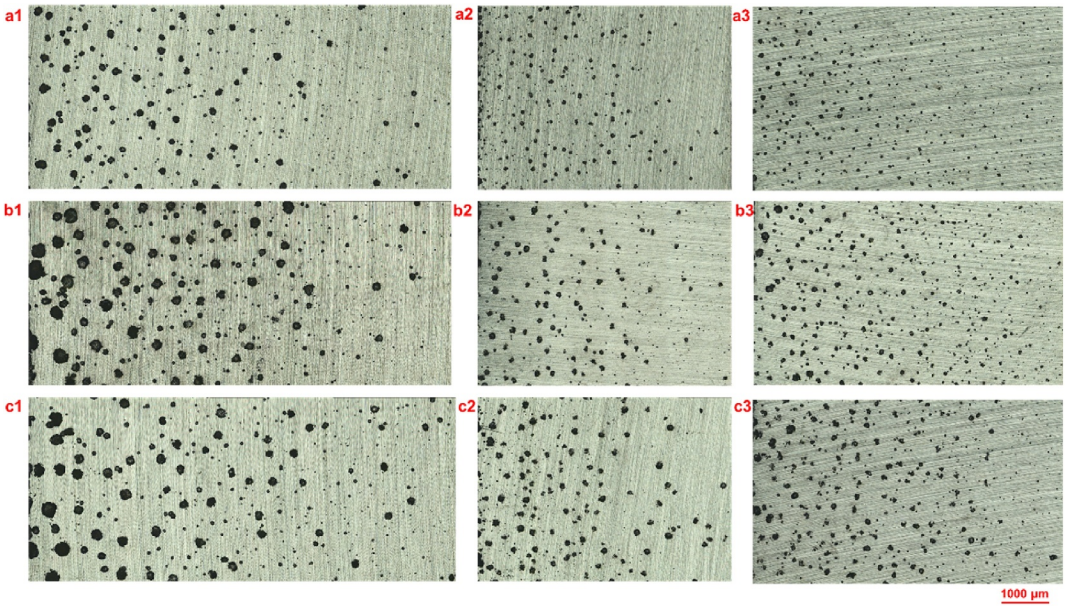

FIGURE 5 Pit coverage area on type 304L BPE (1. FU, 2. PE, and 3. FD) for different exposure time (a) 5 min, (b) 10 min, and (c) 15 min. BPE, bipolar electrode; FD, face down; FU, face up; PE, perpendicular.

potential at each point on the BPE remains nearly constant over time. This means that pit nucleation occurs under potentio-static conditions, leading to different critical pitting potential compared to E_{pit} from potentio-dynamic polarization. In the FU orientation, gravity helps retain the aggressive pit electrolyte inside the pit, thereby reducing the pitting nucleation potential. In contrast, during potentio-dynamic polarization, the exposure time from the metastable pit to E_{pit} is relatively short, limiting the time for pit electrolyte diffusion and making the effect of gravity on pit nucleation negligible. The role of gravity in determining the pitting potential on the BPE is more pronounced for type 420 than that for type 304L stainless steel, as the presence of numerous carbides within type 420 stainless steel, which are the pit nucleation sites.[55] In contrast, type 304L stainless steel has higher Cr and Ni content, resulting in fewer pit nucleation sites and slower pit growth kinetics. The combination of abundant nucleation sites and faster growth in type 420 stainless steel makes it more susceptible to the influence of gravity on pit development.

Figure 6 provides a comparative analysis of pitting corrosion morphology of type 420 and 304L stainless steel with different surface orientations at the same BPE location. Figure 6a1–c1 reveals that all pits in type 420 stainless steel exhibit a circular cross-section. A relatively dark area, referred to as the "pit ring," surrounds the pits, which is caused by general corrosion from the pit electrolyte. The pit ring is smallest in the FD orientation, as gravity facilitates the removal of pit electrolyte. In the PE orientation, the large pits on the BPE are connected by black lines. In the FU orientation, pits are found in close or even in contact with each other, while pits in the PE orientation are slightly more spaced apart. The large pit diameters follow the sequence FU (150 μm) > PE (120 μm) > FD (100 μm). For type 304L stainless steel, as shown in Figure 6a2–c2, the cross-section of large pits in the FU orientation is nearly semi-circular, while smaller, irregularly shaped pits are observed in the PE and FD orientations. The pits in the FU orientation have a flat bottom, with diameters and depths reaching up to 125 and 140 μm, respectively. In contrast, pits in the PE and FD orientations exhibit a sharper bottom, with maximum diameters and depths reduced to 100 and 120 μm, respectively. Compared to pits in the FU orientation, the pit aspect ratio (defined as the ratio of pit depth to width) is larger in the PE and FD orientations, and the pit depth is greater, consistent with the localized solution framework pit growth model.[38]

3.4 | Pit depth, area and volume on the BPE

The areas covered by pits are divided into five sub-regions, each measuring 1 × 4 mm^2 (length × width). Region one is situated in the highest potential region adjacent to the oxidation edge, while Region 5 represents the lowest applied potential, located near the center of BPE. Figure 7 illustrates the deepest pits in BPE at different surface orientations and exposure times. The deepest pit in each region is determined by calculating the average value and standard deviation of the five deepest pits that do not merge or contact with other pits. A linear relationship is established at the pit depth at different BPE regions, where a more negative slope of the equation indicates a greater contribution of the applied potential to pit depth. For stable pits, pit growth is controlled by diffusion, resulting in pit depth being independent of the applied potential. However, for metastable pits, pit depth increases almost linearly with time.[43] Figure 7a1–c1 illustrates the pit volume distribution on the BPE for type 420 stainless steel with FU, PE and FD orientations. The deepest pits are observed in the BPE with the FD orientation, followed by the PE and FU orientations. The slope of pit depth along the BPE with the FU orientation is almost zero, indicating that pit depth is largely independent of the applied potential. In contrast, the largest pit depth slope is observed in the FD orientation, suggesting that local potential significantly influences pit

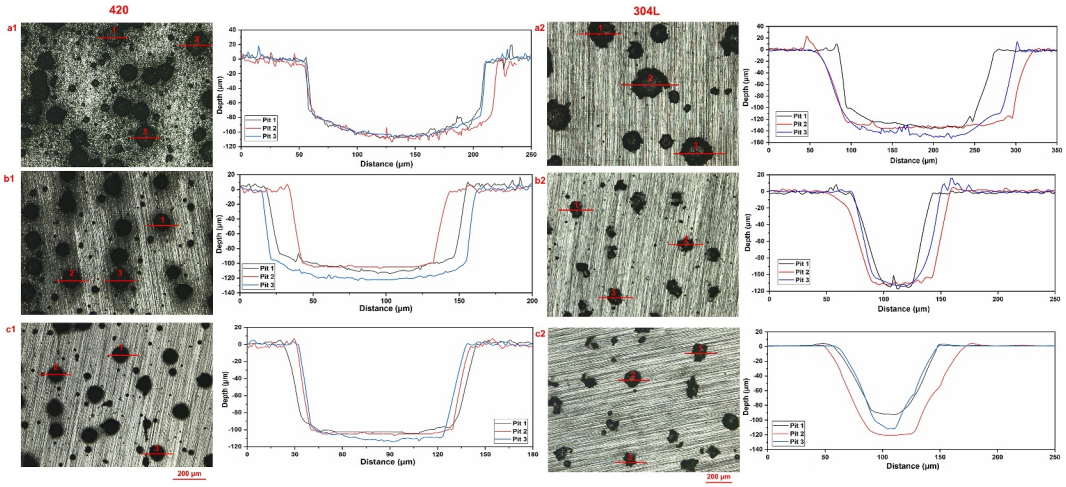

FIGURE 6 The optical images of pitting corrosions region in type 420 (1) and 304L (2) stainless steel in FU (a), PE (b), and FD (c) orientations after 15 min exposure. FD, face down; FU, face up; PE, perpendicular.

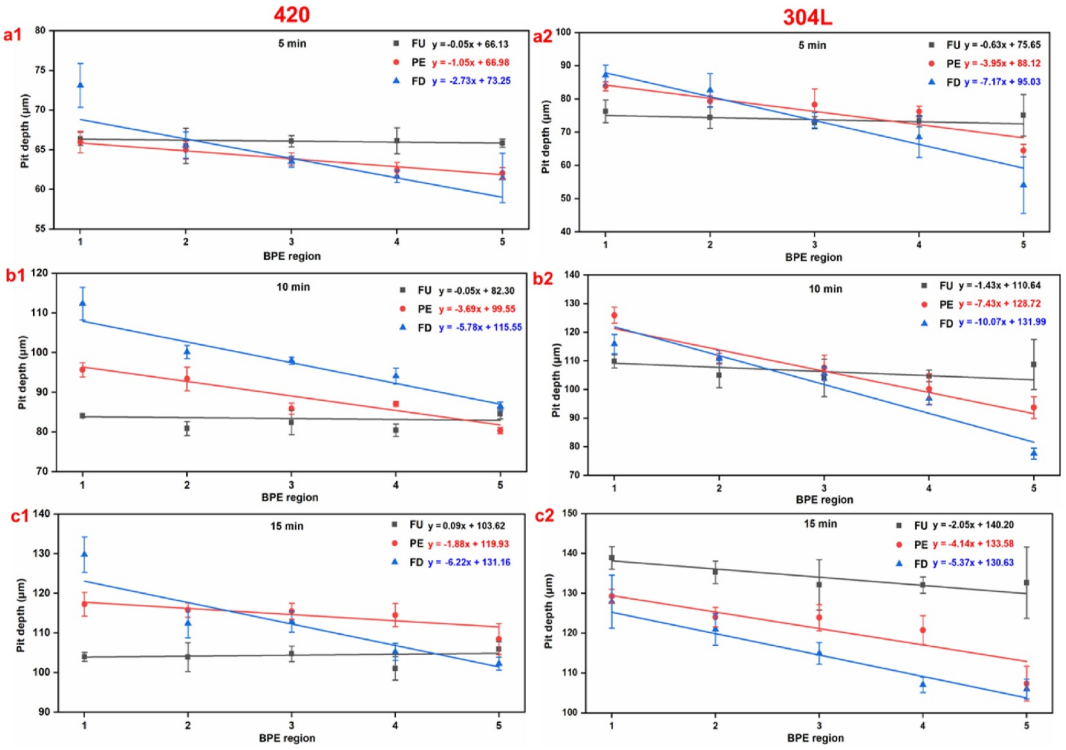

FIGURE 7 Average pit depth along the BPE length with (a) FU, (b) PE, and (c) FD orientation from 5 min to 15 min for type (1) 420 and (2) 304L stainless steel. BPE, bipolar electrode; FD, face down; FU, face up; PE, perpendicular.

growth kinetics in depth direction. For pitting corrosion on type 304L BPE, as shown in Figure 7a2–c2, the smoothest and largest pit depth slopes are detected in the FU orientation, similar to the trends observed in type 420 stainless steel. However, the deepest pits on type 304L BPE vary with exposure time. At 5 and 10 min, the deepest pits are found in the FD and PE orientations, respectively. At 15 min, the deepest pits are observed in the BPE with the FU orientation.

For the FU orientation, the pit depth remains nearly constant from BPE Region 1 to Region 5 for Type 420 and 304L stainless steel across exposure times of 5–15 min. In contrast, for the PE and FD orientations, pit depth increases with higher applied potentials, suggesting that pit growth is not under diffusion control but rather under activation control. Li et al.[56] noted that the current density associated with pit activation growth increases with the applied potential. As a result, pit depth increases from Region 5 to Region 1. Also, diluting pit electrolyte decreases pit growth speed, leading to deeper pits in BPEs with FD and PE orientations. It is also evident that stable pit growth does not necessarily require the formation of a salt film, as pits in the BPE with PE and FD orientations can grow under activation control.[57] Interestingly, for type 304L stainless steel, pits are the deepest in the FD orientation at 5 and 10 min. However, after 15 min, pits in the FU orientation become the deepest. This phenomenon may be attributed to a sudden drop in the ohmic potential of the pit electrolyte relative to pit depth during pit growth under activation control, resulting in lower pit growth kinetics.[38]

In Figure 8a, it is evident that the largest pit cross-sectional area is observed in the BPE with the FU orientation, while the cross-sectional areas in the FD and PE setups are smaller. The relationship between pit cross-sectional area and exposure time appears to be nearly linear for all orientations. The slope of the linear equation is used to compare the pit expansion rates, with a larger slope indicating faster pit cross-sectional area expansion. The slopes of these equations, ranked in descending order, are as follows: FU > FD > PE. Figure 8b depicts the overall pit volume in the BPEs with FU, PE, and FD orientations. The pit growth kinetics are slowest in the PE orientation, resulting in the lowest pit volume loss across all exposure times. In contrast, the largest pit volume loss and the fastest pit volume growth rates are observed in the BPE with the FU orientation. For type 420 stainless steel, as shown in Figure 8c,d, the largest pit cross-sectional area and the greatest pit volume loss are also found in the FU orientation. In the FD orientation, the pit cross-sectional area and pit volume loss are slightly lower than those in the PE orientation.

For type 420 stainless steel BPE, the differences in pit cross-sectional area and pit volume between the FU orientation and the other orientations remain nearly constant over prolonged exposure times. This suggests that the pit growth behavior in type 420 stainless steel is relatively consistent across different surface orientations once stable pit growth is established. In contrast, for type 304L stainless steel, the pit cross-sectional area and pit volume exhibit accelerated growth in the FU orientation compared to the PE and FD orientations. This acceleration is attributed to the increase in

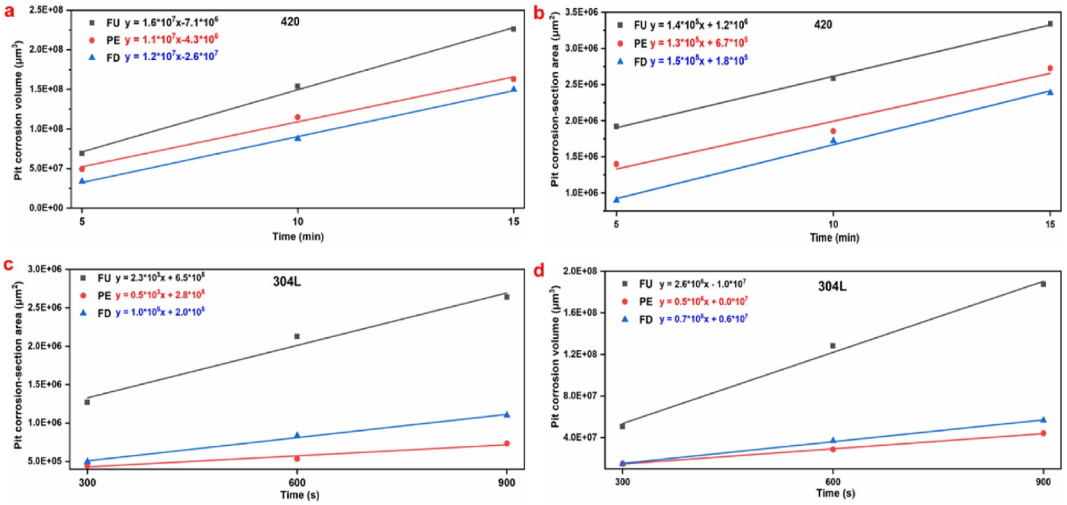

FIGURE 8 Overall cross-section area and volume from the pitting corrosion on (a, b) type 420 and (c, d) type 304L bipolar electrode.

both the number and size of large, continuously growing pits that lose their lacy pit covers after reaching a significant size. Once the lacy pit cover is lost, the contribution of gravity to the diffusion rate becomes more pronounced in the BPE with PE and FD orientations. This results in a slower expansion rate in both the pit wall and pit depth directions, as gravity facilitates the removal of the aggressive pit electrolyte from the surface, reducing the driving force for pit growth. These observations highlight the distinct behaviors for pit growth between type 420 and 304L stainless steel, with the latter showing a stronger dependence on surface orientation and exposure time due to the dynamic nature of lacy pit cover formation and loss.

Figure 9 provides a comparative analysis of the percentage of different pit volumes on type 420 and 304L BPEs over exposure times ranging from 5 to 15 min. Figure 9a–c illustrates the pit volume distribution on type 420 BPEs. At 5 min, the percentage of small pits (volume $<4.0 \times 10^4$ μm^3) in the FD orientation is 39%, which is higher than in the PE (25%) and FU (23%) orientations. The majority of pits (≈50%) have volumes between 1.2×10^5 and 4.0×10^5 μm^3 across all BPE samples. The highest percentage of pits with volumes exceeding 1.6×10^6 μm^3 is observed in the FU orientation. At 10 min, the percentage of pit volumes below 1.2×10^5 μm^3 remains similar to that at 5 min. However, the percentage of pit volumes between 1.2×10^5 and 4.0×10^5 μm^3 decreases, while the concentration of larger pit volumes ($>4.0 \times 10^5$ μm^3) increases significantly. By 15 min, the highest concentration of both the smallest pits ($<4.0 \times 10^4$ μm^3) and the largest pits ($>1.3 \times 10^6$ μm^3) is observed in the type 420 BPE with the FU orientation.

Figure 9d,e demonstrates the pit volume distribution on type 304L BPEs. The lowest concentration of the smallest pits ($<4.0 \times 10^4$ μm^3) and the largest pits ($>4 \times 10^5$ μm^3) is observed in the FU orientation from 5 to 15 min. In contrast, the highest concentration of the smallest and largest pits is consistently found in the FD orientation. These results indicate that the percentage of pits evolving into larger sizes is higher in the FU orientation compared to the PE and FD orientations, particularly for pits with lacy covers during the early stages of pit expansion. This highlights the significant influence of surface orientation on pit growth behavior, with the FU orientation promoting faster and more extensive pit development due to the retention of aggressive pit electrolyte by gravity. Indeed, gravity exerts a dual influence on pitting corrosion behavior. However, an exception to this trend is observed in type 304L stainless steel after 15 min of exposure, where pits in the FU orientation become deeper than those in the PE and FD orientations. This deviation may be attributed to the longer pit growth period after losing pit lacy covers, which alters the overall diffusion dynamics and pit growth kinetics.

3.5 | Pit shapes on the BPE

In single-phase stainless steel, such as Type 316L stainless steel, the transition of pit shape from bottle-like to dish-like as more stable salt film.[58] In contrast, in duplex stainless steels, pit shape is also influenced by the size and morphology of the austenite and ferrite phases.[59–62] To better understand pit morphology, three reference pit shapes are considered, characterized by pit shape factors of 0.5 (open pit), 1 (semi-circular pit), and 2 (narrow pit). The assumption is that, for a constant pit depth, a smaller shape factor corresponds to a larger pit volume. The relationship between the pit depth (d) and pit volume (V) follows Equation (1), where r is the radius of the pit mouth (assume the pit mouth is a circle shape). Equation (2) shows the relationship between the pit depth (d) and pit radius (r), α is a pit shape factor depending on the pit shape.

$$V = \frac{1}{2} \times \frac{4}{3} \times \pi \times d \times r^2, \tag{1}$$

$$d = \alpha \times r. \tag{2}$$

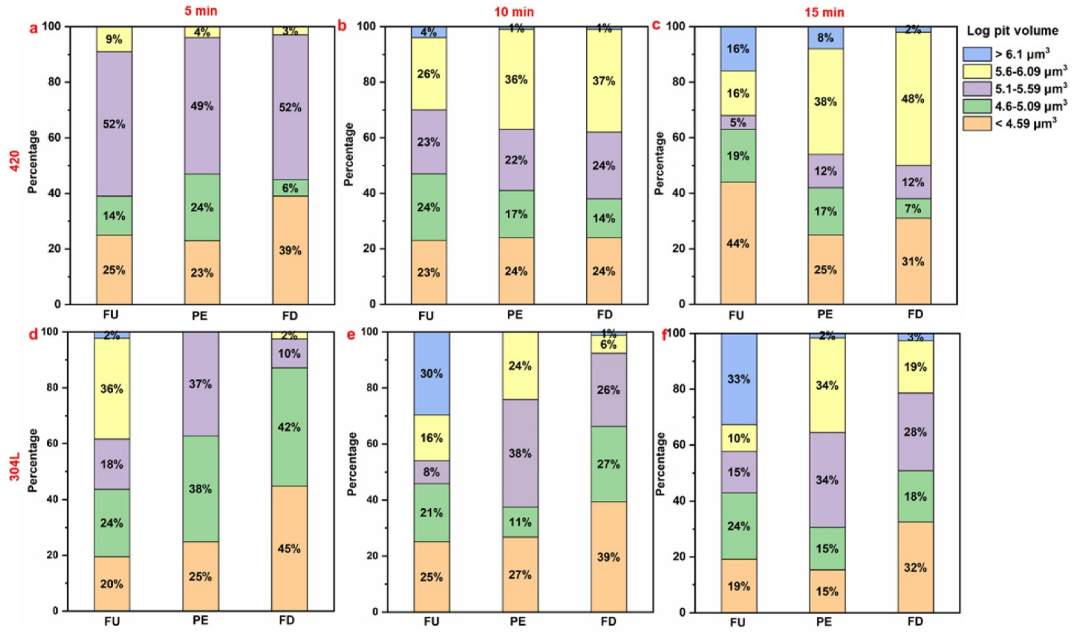

FIGURE 9 Percentage of log pit volume on type (a–c) 420 and (d–f) 304L bipolar electrode from 5 to 15 min with three different surface orientations.

Figure 10 illustrates the correlation between gravity, exposure time, and pit volume on type 420 and 304L BPEs. At 5 min (Figure 10a1), the maximum pit depths in the FU and PE orientations reach up to 70 μm, while the deepest pits in the FD orientation approach over 80 μm. Large pits in the FU orientation exhibit shapes between semi-circular and deep reference lines, whereas pits in the PE and FD orientations follow different patterns. At 10 min (Figure 10b1), the maximum pit depth in the FD orientation increases to 120 μm, which is 10–20 μm deeper than in the FU and PE orientations. Large pits in the FU orientation maintain a semi-circular shape, while those in the PE and FD orientations tend toward a deeper, more narrower shape. By 15 min (Figure 10c1), the pits in the FU orientation become slightly wider, while the pit shapes in the PE and FD orientations remain similar to those observed at 10 min. For type 420 stainless steel, as exposure time increases, the pits in the FU orientation tend to widen, while those in the PE and FD orientations initially deepen during the first 10 min and then stabilize in shape with prolonged exposure.

The evolution of pit depth versus volume on type 304L stainless steel BPEs with different surface orientations and exposure times is illustrated in Figure 10a2–c2. Figure 10a2 reveals that pits in the FU orientation exhibit shapes between semi-circular and dish-like, while those in the PE and FD orientations fall below the deep reference lines. The depth of large pits in the PE and FD orientations is greater than those in the FU orientation. The shape of large pits remains relatively consistent over exposure time for all orientations, while smaller pits tend to have a wider shape compared to larger pits, as shown in Figure 10b2,c2. Interestingly, the deepest pits are observed in the FU orientation after 15 min of exposure. This phenomenon may be attributed to the loss of lacy pit covers in large pits during growth after 10 min, leading to a sudden drop in pit electrolyte concentration and a reduction in the C_{crit} of aggressive species.

Figure 11 illustrates the influence of gravity on pit morphology in type 420 and 304L BPEs after 15 min of exposure at the different regions (Region 1–Region 5). In Figure 11a1,a2, it is observed that the deepest pits, exceeding 100 μm in type 420 stainless steel and 140 μm in type 304L stainless steel, are consistent across all regions. Pits in regions with a higher applied potential are much wider than semi-circular pits, while pits in lower applied potential regions are deeper than semi-circular pits. In Figure 11b1, the majority of large pits in Type 420 BPE with a PE orientation are aligned near the narrow pit shape line, with only a few resembling a semi-circular shape at high applied potentials. Figure 11b2 shows the pit shapes on type 304L BPE with the PE orientation after 15 min of exposure, where all pits fall below the narrow pit shape line, indicating deeper and narrower pit morphologies. Figure 11c1,c2 demonstrate the pits in the FD orientation along the BPE length; the pits in Region 1 are the deepest among all regions for both type 420 and 304L BPEs. The pit shapes in both stainless steels are deeper than the deep shape reference line. Additionally, smaller pits are observed to be wider than larger pits across all applied potential regions, and pits nucleated in lower applied potential regions are deeper than those in higher applied potential regions.

To investigate the evolution of pitting corrosion over an extended period, type 420 stainless steel with FU, PE, and FD orientations was exposed to 0.05 M HCl for 120 min in a bipolar electrochemistry setup. Figure 12a shows that the pit density in the BPE with the FU orientation is significantly

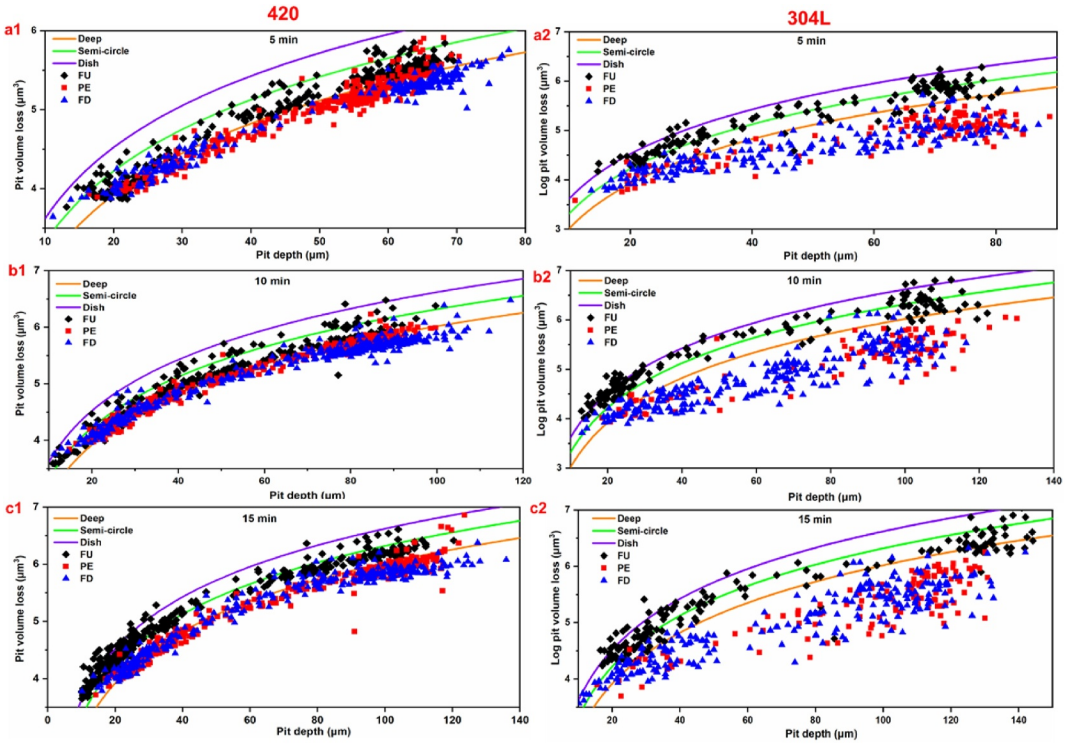

FIGURE 10 Pit depth and volume in type 420 and 304L BPEs with different exposed surface orientations. Type 420 stainless steel runs for (a1) 5 min, (b1) 10 min, and, (c1) 15 min, type 304L BPEs exposed for (a2) 5 min, (b2) 10 min, and (c2) 15 min. BPEs, bipolar electrodes.

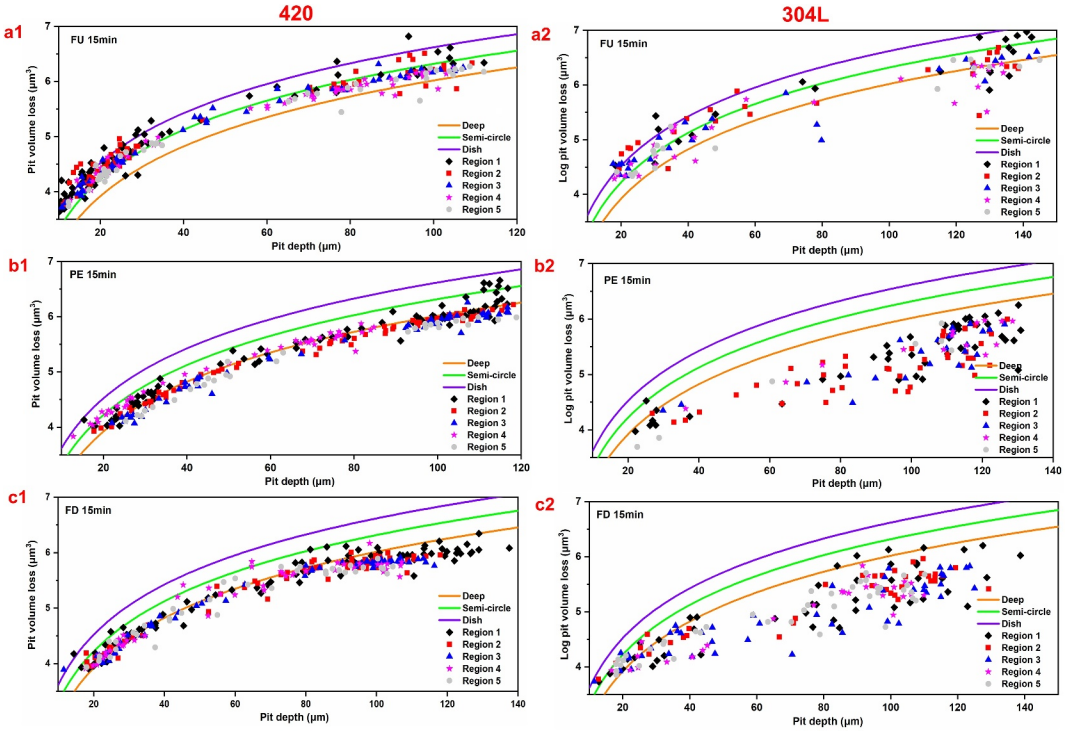

FIGURE 11 Pit shape distribution along the BPE for type (1) 420 and (2) 304L stainless steel with (a) FU, (b) PE, and (c) FD orientation after 15 min exposure. BPE, bipolar electrode; FD, face down; FU, face up; PE, perpendicular.

higher near the BPE oxidation edge compared to the center. A dark area is observed in the region with an elevated applied potential, indicating that general corrosion from the pit electrolyte primarily affects surfaces with sufficient pit density, while the BPE center is relatively bright with visible scratches. In Figure 12b,c, the pit size in the PE and FD orientations is smaller than in the FU orientation. Scratches are clearly visible across BPE regions, and pits in the PE

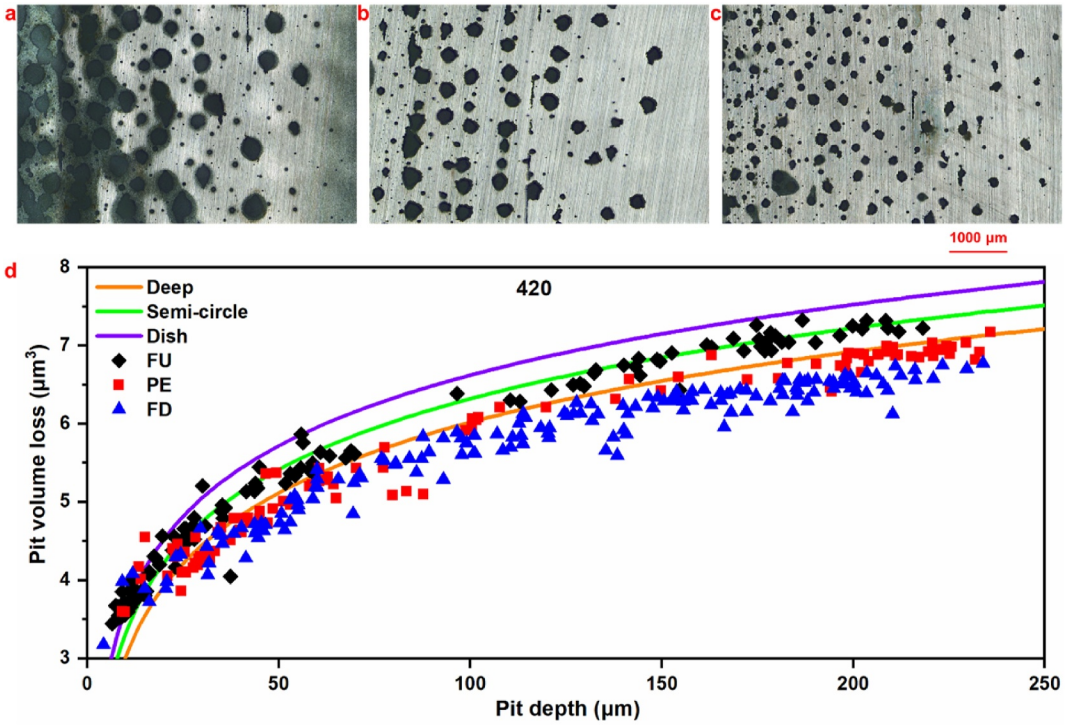

FIGURE 12 Pitting covered on type 420 BPE in (a) FU, (b) PE, and (c) FD orientations after 120 min exposure, with (d) pit shape distribution in these three BPE setups. BPE, bipolar electrode; FD, face down; FU, face up; PE, perpendicular.

orientation exhibit linear alignment along the width of the BPE. Figure 12d reveals that the deepest pits in the PE and FD orientations reach up to 235 μm, while the deepest pits in the FU orientation are <220 μm. Large pits in the FU orientation maintain a semi-circular shape, whereas pits in the PE and FD orientations are narrower, with the narrowest pits observed in the FD orientation. Over the 120-min exposure period, pits in type 420 stainless steel continue to expand, indicating that both activation control and diffusion control mechanisms support pit growth to relatively large volumes and depths. The pit shape remains semi-circular in the FU orientation and deep-like in the PE and FD orientations. Notably, pits in the FD orientation are deeper than those in the PE orientation, as gravity facilitates the dilution of the pit electrolyte in the FD setup.

3.6 | Crystallographic pits

Small, regular crystallographic hexagonal pits (up to 6 μm in size) were observed on type 420 stainless steel with the FU orientation after exposure to 0.1 M HCl for 5 min. Prior to bipolar electrochemistry testing, the samples were polished to a 1 μm finish to ensure a scratch-free surface. Figure 13a shows one of these pits with a flat wall, containing an elliptical Cr carbide. This Cr carbide was exposed as the surrounding matrix corroded away, leaving it inside of the pit. Figure 13b displays hexagonal pits up to 5 μm in size, with slight variations in surface height indicating the presence of general corrosion. Figure 13c,d depicts two circular pits, each approximately 6 μm in size, where Cr carbides are prominently positioned ahead of the matrix, demonstrating their superior corrosion resistance. Numerous carbides were observed within these pits, indicating that the aggressive pit electrolyte was unable to dissolve them, and leading to their accumulation inside the pits (Figure 13d). These crystallographic pits have the potential to grow into larger facet pits (without a salt film) or transform into hemispherical pits with a salt film.[63] The observation of only small crystallographic pits may be due to the transition to a semi-circular shape when pits reach a critical diameter of around 6 μm, marking the transformation from crystallographic to circular pits. Interestingly, previous studies have noted that crystallographic pits typically form at relatively low potentials or current densities.[64] However, in this case, small crystallographic pits were observed in a region of high applied potential, likely due to the generation of many pits. Although these pits initially grew under high current density, their growth was later controlled by charge transfer without the formation of a salt film. As the current density decreased due to pit competition, pit growth was no longer supported, resulting in crystallographic pits.

4 | CONCLUSIONS

Gravity significantly influences pitting corrosion through the dilution of pit electrolyte and the removal of salt films. A novel bipolar electrochemistry method has been developed to evaluate the impact of gravity and potential on pitting

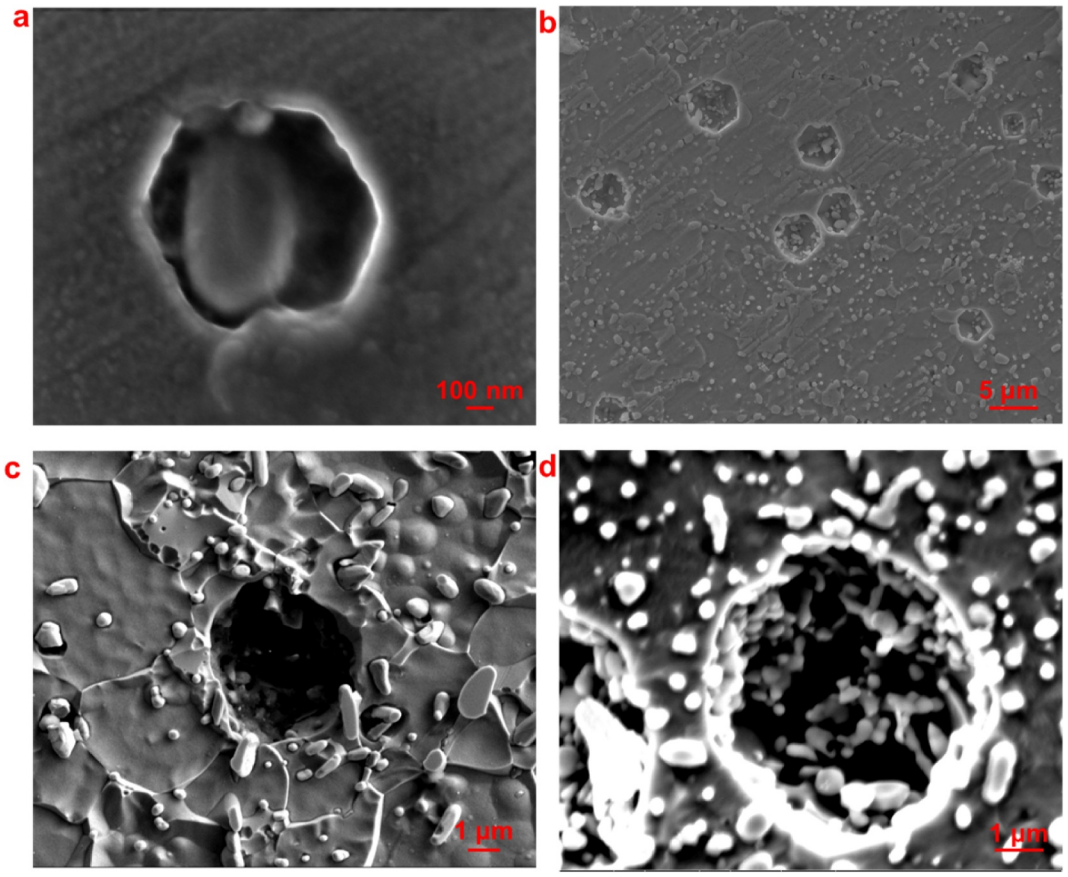

FIGURE 13 (a, b) Hexagonal and (c, d) circle pits detected type 420 BPE with FU orientation tested in 0.1 M HCl for 5 min. BPE, bipolar electrode; FU, face up.

corrosion performance. The main limitations of this research are the relatively short exposure periods (5–120 min) and the specific environmental conditions, such as the use of HCl as the corrosive medium. The main conclusions are as follows:

- The bipolar electrochemistry method creates a linear potential gradient on the BPE, enabling the evaluation of gravity's contribution to pitting corrosion across a wide range of applied potentials. Gravity influences current distribution on the BPE but does not affect potential distribution.
- Pits in the PE and FD orientations are deeper than those in the FU orientation, but the pit volume and cross-sectional area are larger in the FU orientation. Pits in the FU orientation exhibit a more dish-like shape compared to the deeper pits in the PE and FD orientations.
- The salt film at the pit bottom is not a definitive indicator of metastable or stable pit growth. Pits can grow under both activation control and diffusion control. Pit shapes become deeper with longer exposure times and higher applied potentials.
- The crystallographic pits were observed on the BPE at a high-applied potential region. A pit diameter of 5–6 μm may indicate the transition from crystallographic to regular shapes.

AUTHOR CONTRIBUTIONS

Yiqi Zhou: Sample preparation; conceptualization; methodology; validation; formal analysis; investigation; data curation; writing—original draft. **Shuoyang Wang**: Sample preparation; data curation. **Shikang Feng**: Formal analysis; writing—review and editing. **Qingyang Liu**: Formal analysis; writing—review and editing. **Brahim Aissa**: Formal analysis; writing—review and editing. **Hussam Attar**: Formal analysis; writing—review and editing. **Sultan Mahmood**: Formal analysis; writing—review and editing. **Eguchi Kenichiro**: Formal analysis; writing—review and editing.

ACKNOWLEDGMENTS

Y. Z. acknowledges financial support by Science & Technology Fundamental resources investigation program (Grant No. 2022FY101300) and Guangdong Basic and Applied Basic Research Foundation (Grant 2023A1515110926).

CONFLICT OF INTEREST STATEMENT

The authors declare no conflicts of interest.

DATA AVAILABILITY STATEMENT

The data that support the findings of this study are available from the corresponding author upon reasonable request.

ORCID

Yiqi Zhou https://orcid.org/0000-0001-6513-7460

REFERENCES

1. Xu D, Zhang Q, Huo X, Wang Y, Yang M. Advances in data-assisted high-throughput computations for material design. *Mater Genome Eng Adv*. 2023;1:1-32.
2. Xie W, Wang W, Liu Y. On the application of high-throughput experimentation and data-driven approaches in metallic glasses. *Mater Genome Eng Adv*. 2023;1:1-10.
3. Chen Z, Lu D, Cao J, et al. Development of high-throughput wet-chemical synthesis techniques for material research. *Mater Genome Eng Adv*. 2023;1:1-23.
4. Ren C, Ma L, Zhang D, Li X, Mol A. High-throughput experimental techniques for corrosion research: a review. *Mater Genome Eng Adv*. 2023;1:e20.
5. Chen D, Zhou W, Ji Y, Dong C. Applications of density functional theory to corrosion and corrosion prevention of metals: a review. *Mater Genome Eng Adv*. 2025;3:e83.
6. Xie J. Prospects of materials genome engineering Frontiers. *Mater Genome Eng Adv*. 2023;1:e17.
7. Xie J. *Materials Genome Engineering Advances*: a new journal dedicated to digital and intelligent materials research and development. *Mater Genome Eng Adv*. 2023;1:e9.
8. Zhou Y, Stevens N, Engelberg DL. Corrosion electrochemistry with a segmented array bipolar electrode. *Electrochim Acta*. 2021;375:137668.
9. Zhou Y, Huang Z, Wang S, et al. Synergistic improvement of pitting and wear resistance of laser powder bed fusion 420 stainless steel reinforced by size-controlled spherical cast tungsten carbides. *Corros Sci*. 2024;237:112342.
10. Zhou Y, Xu X, Wang S, et al. Optimize the corrosion and mechanical performance of additive manufactured nano-size WC reinforced stainless steel matrix composites by heat treatments, *Mater Corros*. 2025;76:620-639.
11. Zhou Y, Engelberg DL. Accessing the full spectrum of corrosion behaviour of tempered type 420 stainless steel. *Mater Corros*. 2021;72:1718-1729.
12. Zhou Y, Mahmood S, Engelberg DL. A novel high throughput electrochemistry corrosion test method – bipolar electrochemistry. *Curr Opin Electrochem*. 2023;39:101263.
13. Zhou Y, Xu X, Yuan P, et al. Effect of re-melting strategies on pitting corrosion resistance in laser powder bed fusion Ni over-alloyed duplex stainless steel. *Corros Sci*. 2025;257:113278.
14. Zhou Y, Wang W, Li L, et al. Microstructure and corrosion performance of laser powder bed fusion produced duplex stainless steel using Ni over-alloyed mixed powder. *Corros Sci*. 2025;253:113025.
15. Munktell S, Tydén M, Högström J, Nyholm L, Björefors F. Bipolar electrochemistry for high-throughput corrosion screening. *Electrochem Commun*. 2013;34:274-277.
16. Zhou Y, Kablan A, Engelberg DL. Metallographic screening of duplex stainless steel weld microstructure with a bipolar electrochemistry technique. *Mater Char*. 2020;169:110605.
17. Zhou Y, Engelberg DL. Development of a two-dimensional bipolar electrochemistry technique for high throughput corrosion screening. *Mater Genome Eng Adv*. 2024;2:e57.
18. Zhou Y, Yuan P, Kong D, et al. Pitting corrosion performance for additively manufactured spherical WC/W2C-reinforced stainless steels in chloride-containing solution. *Int J Miner Metall Mater*. 2024.
19. Zhou Y, Yuan P, Xu X, et al. The tribo-corrosion performance of laser powder bed fusion WC/W2C reinforced stainless steel in different pH value solution. *Tribol Int*. 2025;206:110596.
20. Zhou Y, Mahmood S, Engelberg DL. High throughput screening of localised and general corrosion in type 2205 duplex stainless steel at ambient temperature. *Int J Miner Metall Mater*. 2023;30:2375-2385.
21. Zhou Y, Mahmood S, Engelberg DL. Bipolar electrochemistry for high throughput screening of localised corrosion in stainless steel rebars. *Constr Build Mater*. 2023;366:130174.
22. Zhou Y, Engelberg DL. Time-lapse observation of pitting corrosion in ferritic stainless steel under bipolar electrochemistry control. *J Electroanal Chem*. 2021;899:115599.
23. Zhou Y, Mahmood S, Engelberg DL. Brass dezincification with a bipolar electrochemistry technique. *Surf Interfaces*. 2021;22:100865.
24. Zhou Y, Huang Z, Kong D, et al. Applying bipolar electrochemistry to assess the corrosion mechanism of HVOF WC-based coatings with varies binders in different environments. *Surf Coat Technol*. 2024;477:130252.
25. Shit G, Mariappan K, Ningshen S. Improvement of sensitization and intergranular corrosion of AISI type 304L stainless steel through thermo-mechanical treatment. *Corros Sci*. 2023;213:110975.
26. Zhou J, Chen Y, Ma Y, et al. Statistical in situ scanning electron microscopy investigation on the failure of oxide scales. *Mater Genome Eng Adv* 2023;1:e12.
27. Kovalov D, Taylor C, Heinrich H, Kelly R. Operando electrochemical TEM, ex-situ SEM and atomistic modeling studies of MnS dissolution and its role in triggering pitting corrosion in 304L stainless steel. *Corros Sci*. 2022;199:110184.
28. Pahlavan S, Moazen S, Taji I, et al. Pitting corrosion of martensitic stainless steel in halide bearing solutions. *Corros Sci*. 2016;112:233-240.
29. Krawczyk B, Cook P, Hobbs J, Engelberg D. Corrosion behavior of cold rolled type 316L stainless steel in HCl-containing environments. *Corrosion*. 2017;73:1346-1358.
30. Chen HC, Sun JL, Yang SL, et al. Thermodynamics and kinetics of isothermal precipitation in magnesium alloys. *Mater Genome Eng Adv*. 2025;3:e86.
31. Zhou Y, Kong D, Wang L, et al. Pit growth kinetics of additively manufactured MoNi over-alloyed type 316L stainless steel. *J Mater Res Technol*. 2023;27:7532-7547.
32. Ryan M, Williams D, Chater R, Hutton B, McPhail D. Why stainless steel corrodes. *Nature*. 2002;415(6873):770-774.
33. Zhou Y, Engelberg DL. Fast testing of ambient temperature pitting corrosion in type 2205 duplex stainless steel by bipolar electrochemistry experiments. *Electrochem Commun*. 2020;117:106779.
34. Soltis J. Passivity breakdown, pit initiation and propagation of pits in metallic materials—review. *Corros Sci*. 2015;90:5-22.
35. Ernst P, Laycock NJ, Moayed MH, Newman RC. The mechanism of lacy cover formation in pitting. *Corros Sci*. 1997;39:1133-1136.
36. Laycock NJ, Moayed MH, Newman RC. Metastable pitting and the critical pitting temperature. *J Electrochem Soc*. 1998;145:2622.
37. Laycock N, Newman R. Localised dissolution kinetics, salt films and pitting potentials. *Corros Sci*. 1997;39:1771-1790.
38. Li T, Scully JR, Frankel GS. Localized corrosion: passive film breakdown vs pit growth stability: part V. Validation of a new framework for pit growth stability using one-dimensional artificial pit electrodes. *J Electrochem Soc*. 2019;166:C3341-C3354.
39. Pistorius PC, Burstein GT. Metastable pitting corrosion of stainless steel and the transition to stability. *Philos Trans Phys Sci Eng*. 1992;341:531-559.
40. Gaudet GT, Mo WT, Hatton TA, et al. Mass-transfer and electrochemical kinetic interactions in localized pitting corrosion. *AIChE J*. 1986;32:949-958.
41. Ernst P, Newman RC. Pit growth studies in stainless steel foils. I. Introduction and pit growth kinetics. *Corros Sci*. 2002;44:927-941.
42. Ernst P, Newman RC. Explanation of the effect of high chloride concentration on the critical pitting temperature of stainless steel. *Corros Sci*. 2007;49:3705-3715.
43. Frankel GS, Stockert L, Hunkeler F, Boehni H. Metastable pitting of stainless steel. *Corrosion*. 1987;43:429-436.
44. Salinas-Bravo VM, Newman RC. An alternative method to determine critical pitting temperature of stainless steel in ferric chloride solution. *Corros Sci*. 1994;36:67-77.

45. Li T, Scully JR, Frankel GS. Localized corrosion: passive film breakdown vs. pit growth stability: part IV. The role of salt film in pit growth: a mathematical framework. *J Electrochem Soc*. 2019;166:C115-C124.
46. Galvele J. Transport processes and the mechanism of pitting of metals. *J Electrochem Soc*. 1976;123:464-474.
47. Gaudet GT, Mo WT, Hatton TA, et al. Mass transfer and electrochemical kinetic interactions in localized pitting norrosion. *AIChE J*. 1986;32:949-958.
48. Wu K, Jung WS, Byeon JW. In-situ monitoring of pitting corrosion on vertically positioned 304 stainless steel by analyzing acoustic-emission energy parameter. *Corros Sci*. 2016;105:8-16.
49. Wu K, Byeon JW. Morphological estimation of pitting corrosion on vertically positioned 304 stainless steel using acoustic-emission duration parameter. *Corros Sci*. 2019;148:331-337.
50. Sato M, Oshikiri Y, Yamada A, Aogaki R. Application of gravity electrode to the analysis of iron-pitting corrosion under vertical gravity field. *Electrochim Acta*. 2005;50:4477-4486.
51. Subramanian C. Localized pitting corrosion of API 5L grade A pipe used in industrial fire water piping applications. *Eng Fail Anal*. 2018;92:405-417.
52. Mankowski J, Szklarska-Smialowska Z. The effect of specimen position on the shape of corrosion pits in an austenitic stainless steel. *Corros Sci*. 1977;17:725-735.
53. Pistorius P, Burstein G. Aspects of the effects of electrolyte composition on the occurrence of metastable pitting on stainless steel. *Corros Sci*. 1994;36:525-538.
54. Zhou Y, Engelberg D. On the application of bipolar electrochemistry to characterise the localised corrosion behaviour of type 420 ferritic stainless steel. *Metals*. 2020;10:1-13.
55. Frankel GS, Li T, Scully JR. Perspective—localized corrosion: passive film breakdown vs pit growth stability. *J Electrochem Soc*. 2017;164:C180-C181.
56. Li T, Scully JR, Frankel GS. Localized corrosion: passive film breakdown vs. pit growth stability: part III. A unifying set of principal parameters and criteria for pit stabilization and salt film formation. *J Electrochem Soc*. 2018;165:C762-C770.
57. Li T, Scully JR, Frankel GS. Localized corrosion: passive film breakdown vs pit growth stability: part II. A model for critical pitting temperature. *J Electrochem Soc*. 2018;165:C484-C491.
58. Zhou Y, Engelberg DL. Application of a modified bi-polar electrochemistry approach to determine pitting corrosion characteristics. *Electrochem Commun*. 2018;93:158-161.
59. Zhou Y, Mahmood S, Lars Engelberg D. Application of bipolar electrochemistry to assess the corrosion resistance of solution annealed lean duplex stainless steel. *Mater Des*. 2023:112145.
60. Zhou Y, Engelberg DL. Application of bipolar electrochemistry to assess the ambient temperature corrosion resistance of solution annealed type 2205 duplex stainless steel. *Mater Chem Phys*. 2022;275:125183.
61. Zhou Y, Kong D, Li R, He X, Dong C. Corrosion of duplex stainless steel manufactured by laser powder bed fusion: a critical review. *Acta Metall Sin*. 2024;37:587-606.
62. Zhou Y, Cao X, Mahmood S, Engelberg DL. A rapid corrosion screening technique for grade 2707 hyper-duplex stainless steel at ambient temperature. *Mater Corros*. 2023;75:227-234.
63. Frankenthal RP, Pickering HW. On the mechanism of localized corrosion of iron and stainless steel: II. Morphological studies. *J Electrochem Soc*. 1972;119:1304.
64. Ke R, Alkire R. Initiation of corrosion pits at inclusions on 304 stainless steel. *J Electrochem Soc*. 1995;142:4056.

How to cite this article: Zhou Y, Wang S, Feng S, et al. Unveiling the influence of gravity on pitting corrosion through advanced high-throughput corrosion test method. *Materials Genome Engineering Advances*. 2025;e70038. https://doi.org/10.1002/mgea.70038